Available online at www.sciencedirect.com
ScienceDirect
Applied Thermal Engineering 27 (2007) 1728–1733
APPLIED THERMAL ENGINEERING
www.elsevier.com/locate/apthermeng

Investigation of two-phase transport phenomena in microchannels using a microfabricated experimental structure

Fu-Min Wang *, Julie E. Steinbrenner, Carlos H. Hidrovo, Theresa A. Kramer, Eon Soo Lee, Sebastien Vigneron, Ching-Hsiang Cheng, John K. Eaton, Kenneth E. Goodson

Mechanical Engineering Department, Stanford University, Room 224, Building 530, Stanford, CA 94305-3030, USA

Received 20 January 2006; accepted 27 July 2006
Available online 27 September 2006

Abstract

Microchannels (0.05–1 mm) improve gas routing in proton exchange membrane fuel cells, but add to the complexities of water management. This work microfabricates experimental structures with distributed water injection as well as with heating and temperature sensing capabilities to study water formation and transport. The samples feature optical access to allow visualization and distributed thermometry for investigation of two-phase flow transport phenomena in the microchannels. The temperature evolution along the channel is observed that the temperature downstream of the distributed water injection decreases as the pressure drop increases. As the water injection rate is lower than 200 μl/min, there exists a turning point where temperature increases as the pressure drop increases further. These micromachined structures with integrated temperature sensors and heaters are key to the experimental investigation as well as visualization of two-phase flow and water transport phenomena in microchannels for fuel cell applications.

Keywords: Microchannel; Two-phase flow; Fuel cells; Microfabrication; Temperature sensor

1. Introduction

The proton exchange membrane fuel cell (PEMFC) is an electrochemical device that converts the chemical energy associated with combining fuel (hydrogen) and oxidizer (oxygen) into electricity with major by-products of water and heat. It is a promising power source for both mobile and stationary applications due to its environmentally friendly attributes as well as its high efficiency.

Studies of water management in the gas delivery system are critical for achieving high performance and longevity of PEMFCs. Currently available polymer electrolyte membranes such as Nafion, sandwiched between the anode (hydrogen supply source) and the cathode (oxygen supply source), need to be hydrated in order to exhibit good proton conductivity. Transport of water inside the membrane occurs due to electro-osmosis, which drags water molecules along with each proton, and back diffusion of water, which is driven by the water concentration gradient set up between the anode and cathode. During PEMFC operation, the membrane can become locally dehydrated and highly resistive if the rate of water transport by electro-osmotic drag is higher than the back diffusion rate; therefore, humidifying the reactant gases can prevent the membrane from drying out. Electrode flooding can occur at the cathode if the rate of water removal by flow advection and back diffusion to the anode fails to keep up with its production and accumulation. Water transport also has an impact on the thermal management of the fuel cell, owing to two phase convection and phase changes in the gas channel. The operating temperature of the cell plays

* Corresponding author. Tel.: +1 650 723 2632; fax: +1 650 723 7657.
E-mail address: fuminmems@gmail.com (F.-M. Wang).

1359-4311/$ - see front matter © 2006 Elsevier Ltd. All rights reserved.
doi:10.1016/j.applthermaleng.2006.07.014

an important role in the evaporation and condensation of the water. Therefore, it is important to characterize the governing thermally induced water transport phenomena in microchannels at the cathode. This motivates the present research which experimentally examines the thermal effects on two-phase flow and water transport in microchannels for fuel cell applications.

The complexities and importance of water management in PEM fuel cells have repeatedly expressed in the literatures [1–7]. However, most studies have focused on the issue of water flow and transport only in the membrane electrolyte assembly (MEA) [8] and gas diffusion layer [9]. Siegel et al. [10] has developed a two dimensional model that includes multi-component and multiphase transport along the gas channel and through the MEA. Very few studies have been directed towards a detailed understanding of the flow behavior in the gas channels, and most are theoretical or computational in nature [11,12]. Furthermore, the influence of thermal effects on the flow behavior and its transport characteristics has not been properly addressed. The management of water is closely connected to the management of heat. Temperature affects the evaporation and condensation of water and significant amounts of heat are transferred during phase changes. Thus, there exists an urgent need for a detailed study of thermally impacted two-phase flow and water transport interactions in mixed surface energy conditions, such as is the case of microchannels in contact with the gas diffusion layer in fuel cells.

In this paper we develop experimental structures microfabricated with distributed water injection as well as heating and temperature sensing capabilities to study thermal effects on two-phase flow in microchannels. Anodic bonding of Pyrex glass on top of silicon substrate provides optical access for visualization. With these micromachined structures we can experimentally investigate and visualize the two-phase flow transport phenomena and temperature evolution in the microchannels. This complements our previous work [13,14] with improved geometries and the addition of the thermal capabilities. This work serves as a foundation for understanding of two-phase flow and water transport in microchannels so that strategies for improving water management can be developed for fuel cell applications.

2. Microfabrication

A schematic view of the experimental structure is shown in Fig. 1. The fabrication process is schematically shown in Fig. 2 and outlined here. Starting with a 400 μm thick double side polished silicon wafer, (a) 1500 Å of thermal oxide is grown as an electrical insulated layer. (b) 0.5 μm of aluminum is deposited and patterned on the back surface as the heaters and resistance temperature detectors (RTDs). (c) 2000 Å of low temperature oxide (LTO) is deposited to protect the heaters and temperature sensors. (d) Oxide is selectively pad-etched to open contacts to heaters and

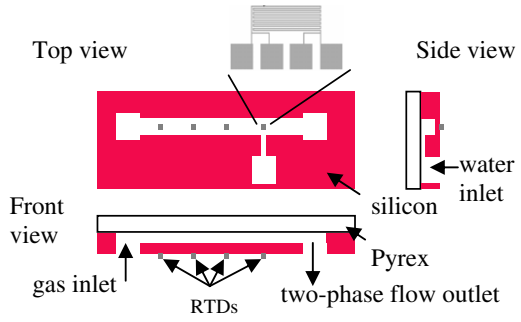

Fig. 1. A schematic top, front and side views of the test structure with single water injection slot.

sensors for wire bonding and to through-etch holes for air/water inlets and outlets. The oxide on the front side is also etched away in this step. (e) Silicon is etched 5 μm deep for water injection channels by deep reactive ion etching (DRIE). (f) Silicon is etched 200 μm deep for air channel using DRIE. (g) Silicon is etched through for air/water inlets and outlets. (h) Pyrex glass is anodically bonded to the top of the silicon to provide optical access of the flow. As microfabricated, the surface of the channel is hydrophilic due to the native oxide layer that grows on the surface of the silicon.

3. Calibration of resistance temperature detectors

Resistance temperature detectors or RTDs are based on the natural change in a metal's resistance with temperature. Calibration needs to be performed on each sensor to find their temperature–resistance dependence before these temperature sensors can be used for quantitative purposes. Temperature calibration of the thin-film aluminum RTDs is performed in a convection oven with a *K*-type thermocouple providing the reference temperature. The sensors are connected in series. A constant current is applied and the voltage drop across each resistor on the test structure is monitored using four point measurements to determine the resistance–temperature correlation of each sensor. The resistance–temperature curves for thin film RTDs are shown in Fig. 3. The sensor sensitivities range between 0.27 Ω/°C and 0.34 Ω/°C as shown in Table 1. RTDs serve as the standard for precision temperature measurements due to their excellent repeatability, stability and linearity characteristics.

The logarithmic derivative, $\partial\rho/\rho\partial T$ or $\partial R/R\partial T$, called the temperature coefficient of resistance (TCR), symbolizes the resistance change factor per degree of temperature change. For pure metals, this coefficient is a positive number, meaning that resistance increases with increasing temperature. It has a value of approximately 0.004/°C when the material (metal or alloy) is pure and free of crystal defects and it has a smaller value when the material is associated with crystal defects, impurities and grain boundaries.

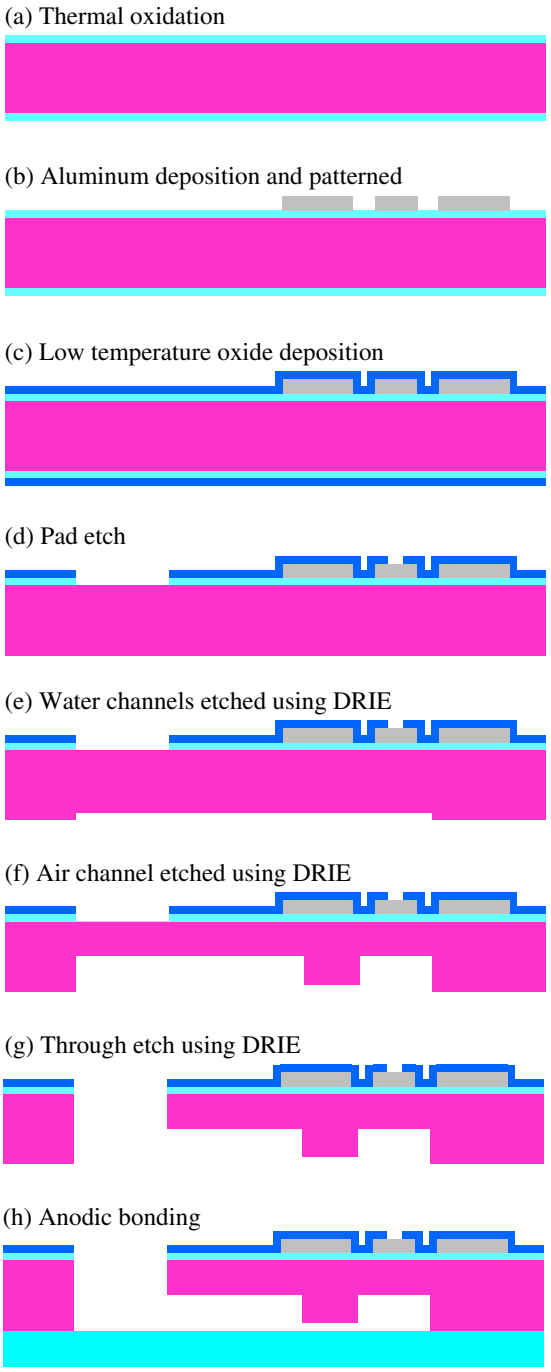

Fig. 2. Microfabrication process: (a) 1500 Å of thermal oxide is grown on a double side polished silicon wafer. (b) 0.5 μm of aluminum is deposited and patterned on the back surface. (c) 2000 Å of LTO is deposited. (d) Oxide is selectively pad-etched to open contact to heaters and sensors. Oxide in the front side is etched away in this step. (e) Silicon is etched 5 μm deep in the front side for water injection channels using deep reactive ion etching (DRIE). (f) Silicon is etched 200 μm deep for air channel using DRIE. (g) Silicon is etched through for air/water inlets and outlets. (h) Pyrex glass is anodically bonded on the top of the silicon.

The TCR of our aluminum temperature sensors is 0.0039/°C indicating that the deposited 0.5 μm thick aluminum film is of good quality.

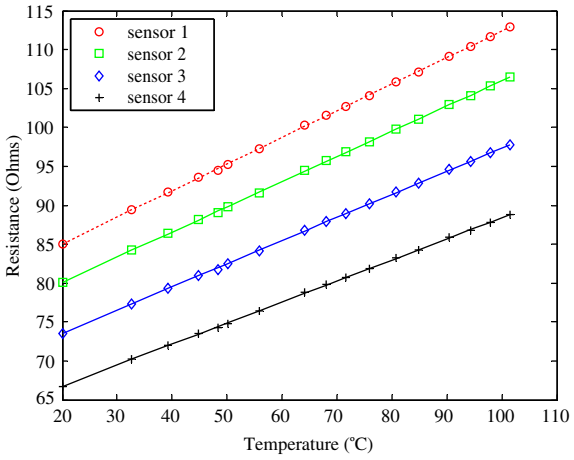

Fig. 3. Calibration curves of temperature sensors showing the resistance of aluminum thin film as a function of temperature with high linearity.

Table 1
Sensitivity and temperature coefficient of resistance associated with temperature sensors

	Sensor 1	Sensor 2	Sensor 3	Sensor 4
Sensivity (Ω/°C)	0.3422	0.3234	0.2973	0.2704
TCR ($°C^{-1}$) at 27 °C	0.0039	0.0039	0.0039	0.0039

4. Self-heating effect

To measure the resistance of a RTD for temperature sensing, a small electric current must flow through the sensor to create the necessary voltage drop. The electric current causes Joule heating and a subsequent increase in temperature. This self-heating depends on the electric power ($P = I^2R$) in the RTD and the heat transfer between the RTD sensing element and the RTD environment. In general, the self-heating effect can be reduced by applying a very small electric current. However, the electric current

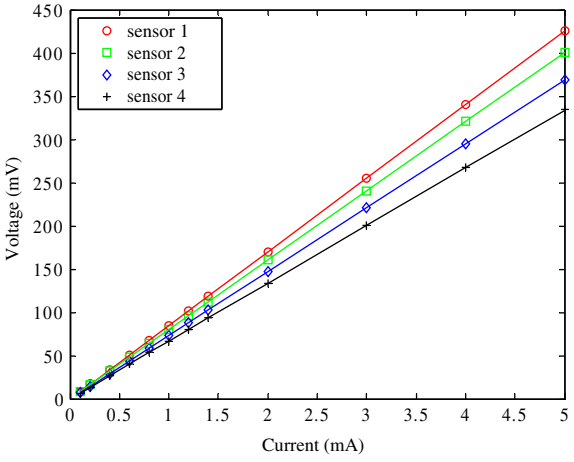

Fig. 4. Current–voltage curve of temperature sensors under constant current.

should be large enough to make the signal (output voltage) meaningful. Fig. 4 shows the voltage–current relationships of the different temperature sensors. Self-heating leads to non-linear curves whose changing slopes arise as a result of the increasing resistance due to Joule heating. The linear relationship between voltage and current is indicative of constant resistance (slope of the curve), and we have verified that the temperature drop due to conduction within the passive materials surrounding the sensor is negligible. Therefore, the self-heating effect can be neglected under these operating currents. The slopes (resistances) are different in similar sensors because of the non-uniformity in thickness as well as variation in width of aluminum temperature sensors.

5. Experimental results

A single microchannel structure for visualization of two-phase flow under distributed water injection from the middle port with integrated temperature sensing is shown in Fig. 5. The structure is 7 cm long, 2 cm wide and 600 μm thick (200 μm Pyrex bonded on 400 μm silicon) with a microchannel on the top side and temperature sensors as well as heater on the back side. Water is injected into the 6 cm long, 500 μm wide, 200 μm deep microchannel from the middle water manifold which consists of 51 5 μm × 5 μm slots spaced by 200 μm. The other two water injection ports are sealed during the experiments. The locations of temperature sensor 1, sensor 2, sensor 3 and sensor 4 are 0.5 cm, 2.5 cm, 4 cm and 5.5 cm downstream of the air inlet as shown in Fig. 5.

The experiments are conducted at room temperature between 20 and 21 °C under different water injection rates and various pressure drops between air inlet and outlet. The inlet air temperature is 22 °C and the outlet was vented to atmosphere conditions. The pressure drop was regulated by increasing the inlet pressure relative to atmosphere conditions. Fig. 6 shows the plot of volume flow rate and mass flow rate against pressure drops ranging from 2 to 45 psi. Both volume and mass flow rates are expressed in standard liters per minute (SLPM). However, mass flow rate has been divided by air density at STP conditions which is 1.293 g/l to express in terms of SLPM for comparison purposes. For very low pressure drops (less than 2 psi), the relationship between inlet volume flow rate and pressure drop is approximately linear, indicating incompressible behavior. As the pressure drop is increased further, the linearity breaks down due to the compressibility of the flow and there is little effect on volume flow rate for pressure drops above 15 psi. This final condition suggests strongly that the flow is choked, i.e., that the volumetric flow rate and flow velocity at the inlet are independent of the pressure drop. The mass flow rate does, however, increase with increasing pressure drop owing to the changing density at the inlet. Theoretically, single phase air flow choking occurs at $P_{out}/P_{in} = 0.528$, which corresponds to the inlet pressure (P_{in}) of 27.8 psi, outlet pressure (P_{out}) of 14.7 psi and pressure difference of 13.1 psi.

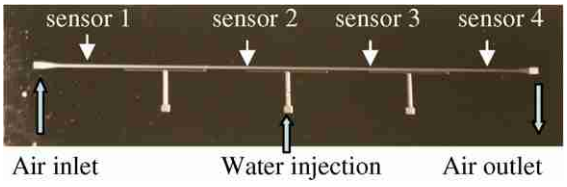

Fig. 5. Top view image of experimental structure showing microchannel, the locations of sensors, air flow direction and water injection port.

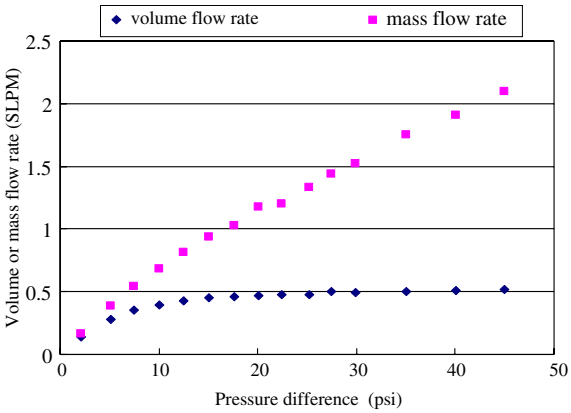

Fig. 6. Volume flow rate and mass flow rate under pressure differences from 2 to 45 psi between air inlet and outlet.

Preliminary temperature measurements have been made with the calibrated temperature sensors. Fig. 7 shows temperature measurements at four locations of the microchannel (0.5 cm, 2.5 cm, 4 cm and 5.5 cm downstream of the air inlet) as a function of pressure drops ranging from 2 to 45 psi with no water injection (single phase air flow). The temperature is decreasing along the microchannel for pressure drops below 10 psi and it is relatively constant along the microchannel under pressure drop above 12.5 psi where it has reached choking conditions.

When water is introduced through the middle injection manifold at a rate of 500 μl/min, the temperature profiles

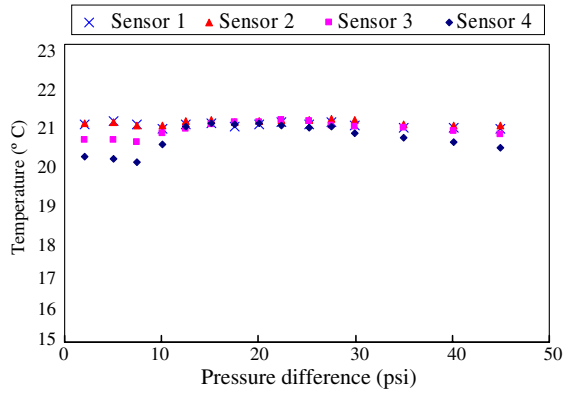

Fig. 7. Temperature measured at four locations of the microchannel (0.5 cm, 2.5 cm, 4 cm and 5.5 cm away from the air inlet) under pressure differences from 2 to 45 psi without water injection.

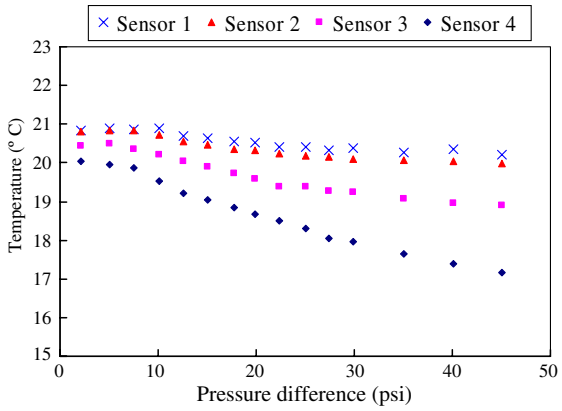

Fig. 8. Temperature measured at four locations of the microchannel (0.5 cm, 2.5 cm, 4 cm and 5.5 cm away from the air inlet) under pressure differences from 2 to 45 psi with room temperature water injection rate of 500 μl/min.

along the microchannel change. Fig. 8 shows that the temperatures upstream of the water injection (sensor 1 and 2) remain nearly equal when water is injected. However, the temperatures downstream of the water injection section (sensor 3 and 4) decrease as the pressure drop increases when water is injected at a rate of 500 μl/min at room temperature. A possible explanation of this phenomenon is evaporative cooling of the wall. A similar trend is observed when hot water (80 °C) is injected at a rate of 500 μl/min as shown in Fig. 9. The temperatures decrease as the pressure drop increases but the temperatures are slightly higher than the room temperature case. There is no substantial difference in temperatures when 80 °C water is supplied since silicon has a high thermal conductivity which allows the water to cool down prior to microchannel injection.

Another interesting phenomenon is observed when water is injected at a rate of 100 μl/min. Under these conditions, temperatures in the downstream of the distributed water injection section (sensor 3 and 4) decrease as the pressure drop increases up to 30 psi. However, when the pressure increases further, the declining temperature phenomenon disappears and the downstream temperature (sensor 3 and 4) increases as shown in Fig. 10. From the in situ water film visualization, it was observed that the water film thickness decreases as pressure drop increases. It was inferred that the evaporative cooling effect diminishes at pressure drops above 30 psi due to the disappearance of the liquid film. This hypothesis requires further modeling and investigation.

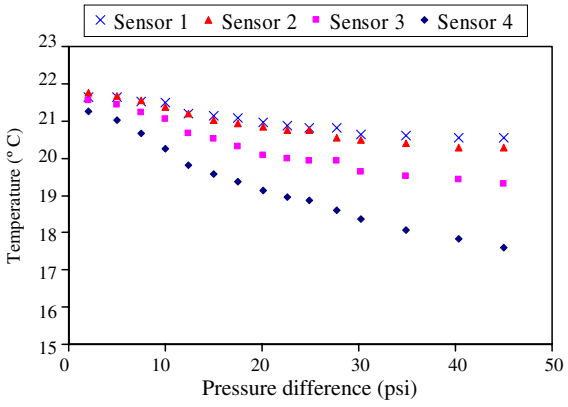

Fig. 9. Temperature measured at four locations of the microchannel (0.5 cm, 2.5 cm, 4 cm and 5.5 cm away from the air inlet) under pressure differences from 2 to 45 psi with 80 °C water injection rate of 500 μl/min.

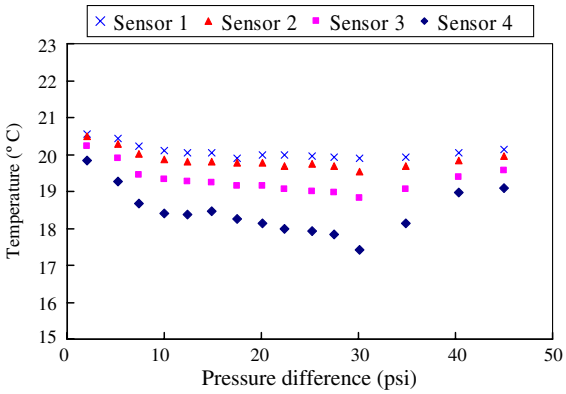

Fig. 10. Temperature measured at four locations of the microchannel (0.5 cm, 2.5 cm, 4 cm and 5.5 cm away from the air inlet) under pressure differences from 2 to 45 psi with room temperature water injection rate of 100 μl/min.

6. Concluding remarks

Experimental structures with heating and temperature sensing capabilities have been fabricated and calibrated for the investigation of two-phase flow transport in microchannels for the specific case of liquid injection. An observed temperature evolution along the channel may be caused by evaporation of the liquid. Further study and model development are needed in order to validate these experimental results, and to take advantage of the metrology enabled by this new device. For example, visual inspection of the two-phase flow through the Pyrex cover is aiding with water film thickness measurements and flow regime characterization as functions of surface hydrophobicity and water injection conditions. This work serves as a foundation for the understanding of two-phase flow and water transport in microchannels so that strategies for improving water management can be developed for fuel cell applications.

Acknowledgements

The authors would like to thank our sponsor, Honda R&D Co. Ltd., not only for their support but also for their input, feedback and insight into the project. Work was performed in part at the Stanford Nanofabrication Facility (a member of the National Nanofabrication Users' Network) which is supported by the National Science Foundation, its lab members, and the industrial members of the Stanford Center for Integrated Systems.

References

[1] T.F. Fuller, J. Newman, Water and thermal management in solid-polymer-electrolyte fuel cells, J. Electrochem. Soc. 140 (5) (1993) 1218–1225.

[2] T. Nguyen, R. White, A water and heat management model for proton-exchange-membrane fuel cells, J. Electrochem. Soc. 140 (8) (1993) 2178–2186.

[3] T.A. Zawodzinski, T.E. Springer, J. Davey, R. Jestel, C. Lopez, J. Valerio, S. Gottesfeld, A comparative study of water uptake by and transport through ionomeric fuel cell membranes, J. Electrochem. Soc. 140 (7) (1993) 1981–1985.

[4] M.L. Perry, T.F. Fuller, A historical perspective of fuel cell technology in the 20th century, J. Electrochem. Soc. 149 (7) (2002) S59–S67.

[5] P. Berg, K. Promislow, J.St. Pierre, J. Stumper, B. Wetton, Water management PEM fuel cells, J. Electrochem. Soc. 151 (3) (2004) A341–A353.

[6] Z.H. Wang, C.Y. Wang, K.S. Chen, Two-phase flow and transport in the air cathode of PEM fuel cells, J. Power Source 94 (2001) 40–50.

[7] L. You, H. Liu, A two-phase flow and transport model for the cathode of PEM fuel cells, Int. J Heat Mass Transf. 45 (2002) 2277–2287.

[8] T.E. Springer, T.A. Zawodzinski, S. Gottesfeld, Polymer electrolyte fuel cell model, J. Electrochem. Soc. 138 (8) (1991) 2334–2341.

[9] U. Pasaogullari, C.Y. Wang, Liquid water transport in gas diffusion layer of polymer electrolyte fuel cells, J. Electrochem. Soc. 151 (3) (2004) A399–A406.

[10] N.P. Siegel, M.W. Ellis, D.J. Nelson, M.R. von Spakovsky, A two-dimensional computational model of a PEMFC with liquid water transport, J. Power Source 128 (2004) 173–184.

[11] J. Yuan, M. Rokni, B. Sundén, Simulation of fully developed laminar heat and mass transfer in fuel cell ducts with different cross section, Int. J. Heat Mass Transf. 44 (2001) 4047–4058.

[12] J. Yuan, M. Rokni, B. Sundén. Modeling of two-phase flow in a cathode duct of PEM fuel cells, in: The First International Conference on Fuel Cell Science, Eng. Technol., Rochester NY, April 21–23, 2003, pp. 463–470.

[13] C.H. Hidrovo, F.-M. Wang, E.S. Lee, J. Paidipati, J.E. Steinbrenner, T.A. Kramer, J.K. Eaton, K.E. Goodson, Experimental investigation and visualization of two-phase flow and water transport, in: Microchannels, ASME International Mechanical Engineering Congress and Exposition, Anaheim, CA, November 13–19, 2004.

[14] S. Vigneron, C.H. Hidrovo, F.-M. Wang, E.-S. Lee, J.E. Steinbrenner, T.A. Kramer, J.K. Eaton, K.E. Goodson, 1D homogeneous modeling of microchannel two-phase flow with distributed liquid water injection from walls, in: ASME International Mechanical Engineering Congress and Exposition, Anaheim, CA, November 13–19, 2004.